



# On fully-implicit solutions of the time-linearized Euler equations in a DG-Chimera solver

Nathan A. Wukie\* and Paul D. Orkwis†

*University of Cincinnati, Cincinnati, Ohio, 45221*

This work demonstrates fully-implicit solutions of the time-linearized Euler equations using a discontinuous Galerkin discretization on Chimera overset grids. Solutions are obtained via a single linear system solve. The linear system matrix is generated with an intrinsic automatic differentiation capability that computes the linear system in the context of Newton's method while evaluating the system residual. A flexible implementation of the Generalized Minimum Residual algorithm coupled with a block-ILU0 preconditioner is used to solve the linear system. Results include a simulation of acoustic scattering off multiple rigid geometries and also acoustic radiation from a cylindrical duct using Kirchhoff's method to compute the observed noise at far-field locations. For the acoustic scattering case, excellent comparison was observed between the numerical and analytical solutions for surface pressure on the rigid geometries. For the cylindrical duct case, the directivity of unsteady pressure for the numerical solution was compared to the analytical solution in the far-field. The directivity patterns were well-matched for several duct modes, however the numerical solution was attenuated due to low grid resolution. A lack of parallelism in the current code prohibited more refined numerical calculations due to memory constraints.

## Nomenclature

$Q$	Solution variable
$\hat{q}$	Complex perturbation variable
$\vec{F}$	Flux vector
$\vec{F}^*$	Numerical flux vector
$\psi$	Legendre basis polynomial
$R$	Spatial residual vector
$S$	Source function
$\vec{n}$	Normal vector
$t$	Time
$\omega$	Angular frequency
$c$	Speed of sound

## I. Introduction

THE linearized Euler equations have been a useful tool for computing unsteady fluid phenomena associated with unsteady turbomachinery aerodynamics and acoustics as well as the propagation of general acoustic data for investigating far-field transmission of acoustic radiation.<sup>1,2</sup> The time-linearized Euler equations take advantage of advanced knowledge of the flow phenomena of interest in assuming a harmonic form for the unsteadiness. This can provide a significant computational advantage over time-marching techniques.

The discontinuous Galerkin(DG) method for solving partial differential equations has been applied in many fields including acoustics, numerical weather prediction, and aerodynamics.<sup>3-5</sup> Part of the strength

\*PhD Student, Dept. of Aerospace Engineering, ML 70, Cincinnati, Ohio 45221, AIAA Student Member.

†Bradley Jones Professor, Dept. of Aerospace Engineering, ML 70, Cincinnati, Ohio 45221, AIAA Associate Fellow.

of the method exists in its ability to provide arbitrarily high-order accuracy, while maintaining a local computational stencil. It also benefits from taking advantage of a great body of work from the Finite Volume community in its use of numerical fluxes to couple the solution between discontinuous elements.

## I.A. Implicit, DG-Chimera framework

Previous work was completed on an implicit, DG framework that uses Chimera overset grids for representing complex geometry and Newton's method for solving nonlinear systems of equations.<sup>6</sup> The framework was implemented with an intrinsic automatic differentiation capability which greatly reduces the effort required to implement new equation sets and boundary conditions while still maintaining Newton convergence of the implicit scheme.

### I.A.1. Chimera gridding capability

The DG method is often used with unstructured computational grids because of its local scheme. However, the properties of DG are also very attractive for Chimera overset grids. Galbraith<sup>7</sup> developed an implicit, DG-Chimera solver that highlighted the benefits of DG applied to Chimera overset grids. This included the elimination of orphan nodes and fringe points that traditionally exist in Finite Volume-based Chimera solvers. Additionally, the ability of DG to accommodate curved geometry solved a Finite Volume issue with overlapping grids, where a boundary from one grid can exist inside the computational domain of a neighbor grid. This makes the DG-Chimera method quite attractive as a framework for a design tool, as it brings together the desired traits of a high-order accurate solution with straight-forward geometry representation and modification.

### I.A.2. Automatic differentiation capability

Newton's method, a technique for solving *nonlinear* sets of equations, requires a linearization of the spatial scheme to compute the update in the solution state. The framework used in this work utilizes an intrinsic automatic differentiation capability based on operator-overloading to automatically compute the linearization matrix  $\frac{\partial R}{\partial Q}$  during the evaluation of the spatial residual  $R(Q)$ . This is advantageous in a development context because it requires that developers only implement the spatial residual(right-hand side). Traditionally, the linearization matrix would have to be derived, implemented, and verified for each new set of equations. The automatic differentiation technique eliminates this cumbersome and error-prone step.

The fully-implicit solution of the time-linearized Euler equations requires the generation of a linear system of equations. This is implemented in the context of the automatic differentiation capability for Newton's method. As such, only the spatial residual for the time-linearized Euler equations is required to be implemented. The matrix for the linear system is computed automatically. Solving the system can be viewed as a single step of Newton's method, which happens to fully converge the discretized governing equations because they are linear.

## I.B. Fully-implicit, time-linearized Euler calculations

The linearized Euler equations can be used to compute unsteady flow phenomena in the form of perturbations about a fixed mean flow. As long as the unsteady perturbations are sufficiently small, the linearized assumption is a valid one. One side-effect of the linear assumption is that the linearized Euler equations admit an instability under certain flow conditions, which is normally damped out by nonlinear flow effects. Agarwal et al.<sup>8</sup> proposed that the equations be solved in the frequency domain, thereby eliminating the mechanism by which the instability could arise. The time-linearized formulation(frequency-domain) of the Euler equations provides an additional computational benefit over the standard time-marching method by solving instead for Fourier coefficients instead of a full time-history of the flow.

There are two methods by which the time-linearized Euler equations can be solved. The first method adds a pseudo-time term to the time-linearized equations and then the solution is marched in pseudo-time until the Fourier coefficients have converged. However as noted by Agarwal et al.,<sup>8</sup> the introduction of the pseudo-time term allows the undesired instability to be reintroduced. Campobasso and Giles<sup>9</sup> advocated the use of the Generalized Minimum Residual(GMRES) algorithm as an iterative solver to stabilize the pseudo time-stepping technique. The second solution method is the fully-implicit technique, which forms a linear system of equations that are solved or inverted to obtain the solution. Since the governing equations are linear, the

converged solution is obtained after a single step. Rao and Morris<sup>10</sup> detail the time-linearized Euler equations solved using the discontinuous Galerkin method as well as the streamline upwind Petrov-Galerkin method. Their conclusion was that the DG method was too expensive when considering the memory requirements. Iob et al.<sup>2</sup> implemented the time-linearized Euler equations using a continuous Galerkin discretization to reduce memory requirements and solved the linear system using a direct solver.

### I.C. Current research

The present work demonstrates a fully-implicit implementation of the time-linearized Euler equations in a DG-Chimera solver. The fully-implicit implementation enables solutions to be computed by solving a linear system of equations that is constructed in the context of Newton's method. The linear system is solved using GMRES with a block-ILU0 preconditioner, which is more memory efficient than a direct solver. This is enabled by an intrinsic automatic differentiation technique which computes the linearization of the spatial scheme, including boundary conditions. This technique drastically reduces the time required to implement and test new methods such as nonreflecting boundary conditions since only the effect of an operator on the residual vector is required. The DG discretization enables accurate computation of wave propagation phenomena and the Chimera grid capability allows nontrivial geometries to be efficiently represented. Previously cited concerns regarding memory requirements are valid, but not insurmountable.

## II. Numerical methodology

The following discussion details the numerical methodology for this investigation, including the discontinuous Galerkin discretization, governing equation set, boundary conditions, and solution technique. See Wukie et al.<sup>6</sup> for a more complete discussion of the framework.

### II.A. The discontinuous Galerkin discretization

The framework is designed to handle equation sets in conservation form as

$$\frac{\partial \mathbf{Q}}{\partial t} + \nabla \cdot \vec{F}(\mathbf{Q}) + S(\mathbf{Q}) = 0 \quad (1)$$

The solution variables are expressed as an expansion in basis functions constructed using a tensor product of one-dimensional Legendre polynomials as

$$\mathbf{Q}(t, x, y, z) = \sum_{i=0}^N \sum_{j=0}^N \sum_{k=0}^N \mathbf{Q}_{ijk}(t) \psi_i(x) \psi_j(y) \psi_k(z) \quad (2)$$

Multiplying by a column of test functions  $\psi$  and applying Gauss' Divergence Theorem gives our working form of the discontinuous Galerkin method as

$$\int_{\Omega_e} \psi \frac{\partial \mathbf{Q}}{\partial t} d\Omega + \int_{\Gamma_e} \psi \vec{F}^* \cdot \vec{n} d\Gamma - \int_{\Omega_e} \nabla \psi \cdot \vec{F} d\Omega + \int_{\Omega_e} \psi S d\Omega = 0 \quad (3)$$

Numerical Gauss-Legendre quadrature is used to compute the spatial integrals in Equation 3. Specialization of this method for a particular set of equations requires the definition of solution variables  $\mathbf{Q}$ , the flux vector  $\vec{F}$ , a choice of numerical flux  $\vec{F}^*$ , and any additional source terms  $S$ . These components are defined for the linearized-Euler equations in the following section.

### II.B. Linearized Euler equations for linear, time-harmonic flows

The time-linearized Euler equations are based on the assumption that the unsteady flow exists as small, harmonic perturbations of the working variables about a steady mean flow as

$$\mathbf{Q}(\vec{x}, t) = \bar{\mathbf{q}}(\vec{x}) + \mathbf{q}'(\vec{x}, t) = \bar{\mathbf{q}}(\vec{x}) + \hat{\mathbf{q}}(\vec{x}) e^{i\omega t} \quad (4)$$

where  $\hat{\mathbf{q}}$  is the complex amplitude of oscillation. The governing equations then take the form of a set of constant-coefficient, linear, partial differential equations as

$$i\omega\hat{\mathbf{q}}(\vec{x}) + \nabla \cdot \frac{\partial \vec{F}(\bar{\mathbf{q}})}{\partial \bar{\mathbf{q}}} \hat{\mathbf{q}}(\vec{x}) = 0 \quad \rightarrow \quad S_t(\hat{\mathbf{q}}, \omega) + \nabla \cdot \vec{F}(\bar{\mathbf{q}}, \hat{\mathbf{q}}) = 0 \quad (5)$$

where  $S_t(\hat{\mathbf{q}}, \omega)$  is a source term induced by the assumed time-harmonic unsteadiness. Here, the term  $\frac{\partial \vec{F}}{\partial \bar{\mathbf{q}}}$  is the constant flux jacobian matrix computed from the nonlinear, steady mean flow. This term is absorbed into  $\vec{F}(\bar{\mathbf{q}}, \hat{\mathbf{q}})$ , which is the flux for the time-linearized Euler equations. By considering the real and imaginary components of the harmonic variables separately, the governing equations can be separated into two sets of perturbation equations as

$$\begin{aligned} -\omega[Im(\hat{\mathbf{q}}(\vec{x}))] + \nabla \cdot \frac{\partial \vec{F}(\bar{\mathbf{q}})}{\partial \bar{\mathbf{q}}} Re(\hat{\mathbf{q}}(\vec{x})) &= 0 \\ \omega[Re(\hat{\mathbf{q}}(\vec{x}))] + \nabla \cdot \frac{\partial \vec{F}(\bar{\mathbf{q}})}{\partial \bar{\mathbf{q}}} Im(\hat{\mathbf{q}}(\vec{x})) &= 0 \end{aligned} \quad (6)$$

The source term and flux matrices used in this work are given in the following sections.

### II.B.1. Cartesian formulation

The time-linearized Euler equations can be recast in primitive variable form in Cartesian coordinates as

$$S_t + A_x \frac{\partial \hat{\mathbf{q}}}{\partial x} + A_y \frac{\partial \hat{\mathbf{q}}}{\partial y} + A_z \frac{\partial \hat{\mathbf{q}}}{\partial z} + S_g + S_u = 0 \quad (7)$$

where  $S_t$  is a source-term due to the time-harmonic unsteadiness,  $S_g$  is a source-term due to mean flow derivatives, and  $S_u$  is used to impose custom source distributions. In this work, the mean flow is assumed to be uniform so we set  $S_g = 0$ . The specific formulation of the flux and source terms used in the discontinuous Galerkin scheme are defined as

$$\vec{F} = [F_x, F_y, F_z] = [A_x \hat{\mathbf{q}}, A_y \hat{\mathbf{q}}, A_z \hat{\mathbf{q}}] \quad (8)$$

$$\begin{aligned} S_t(\hat{\mathbf{q}}, \omega) &= \begin{bmatrix} i\omega & 0 & 0 & 0 & 0 \\ 0 & i\omega & 0 & 0 & 0 \\ 0 & 0 & i\omega & 0 & 0 \\ 0 & 0 & 0 & i\omega & 0 \\ 0 & 0 & 0 & 0 & i\omega \end{bmatrix} \begin{bmatrix} \hat{\rho} \\ \hat{u} \\ \hat{v} \\ \hat{w} \\ \hat{p} \end{bmatrix}, & F_x(\bar{\mathbf{q}}, \hat{\mathbf{q}}) &= \begin{bmatrix} \bar{u} & \bar{\rho} & 0 & 0 & 0 \\ 0 & \bar{u} & 0 & 0 & \frac{1}{\bar{\rho}} \\ 0 & 0 & \bar{u} & 0 & 0 \\ 0 & 0 & 0 & \bar{u} & 0 \\ 0 & \gamma \bar{p} & 0 & 0 & \bar{u} \end{bmatrix} \begin{bmatrix} \hat{\rho} \\ \hat{u} \\ \hat{v} \\ \hat{w} \\ \hat{p} \end{bmatrix}, \\ F_y(\bar{\mathbf{q}}, \hat{\mathbf{q}}) &= \begin{bmatrix} \bar{v} & 0 & \bar{\rho} & 0 & 0 \\ 0 & \bar{v} & 0 & 0 & 0 \\ 0 & 0 & \bar{v} & 0 & \frac{1}{\bar{\rho}} \\ 0 & 0 & 0 & \bar{v} & 0 \\ 0 & 0 & \gamma \bar{p} & 0 & \bar{v} \end{bmatrix} \begin{bmatrix} \hat{\rho} \\ \hat{u} \\ \hat{v} \\ \hat{w} \\ \hat{p} \end{bmatrix}, & F_z(\bar{\mathbf{q}}, \hat{\mathbf{q}}) &= \begin{bmatrix} \bar{w} & 0 & 0 & \bar{\rho} & 0 \\ 0 & \bar{w} & 0 & 0 & 0 \\ 0 & 0 & \bar{w} & 0 & 0 \\ 0 & 0 & 0 & \bar{w} & \frac{1}{\bar{\rho}} \\ 0 & 0 & 0 & \gamma \bar{p} & \bar{w} \end{bmatrix} \begin{bmatrix} \hat{\rho} \\ \hat{u} \\ \hat{v} \\ \hat{w} \\ \hat{p} \end{bmatrix} \end{aligned} \quad (9)$$

where  $\hat{\mathbf{q}} = [\hat{\rho} \ \hat{u} \ \hat{v} \ \hat{w} \ \hat{p}]^T$  and  $[u, v, w]$  are the Cartesian velocity components  $[U_x, U_y, U_z]$ .

### II.B.2. Boundary conditions

Boundary conditions are imposed weakly through the boundary flux integral in Equation (3). The approach taken here is to construct a boundary condition solution state  $\hat{\mathbf{q}}_{bc}$  and then the boundary flux is computed as  $\vec{F}(\hat{\mathbf{q}}_{bc})$  using the definition in Equation (9).

Inlet boundary conditions were imposed using a 1D characteristic-based technique. In this method, the incoming characteristics are computed from user-specified perturbations at the inlet. The outgoing characteristics are computed from the interior solution. The solution on the boundary that is used to compute the flux is composed from the computed incoming and outgoing characteristics. The transformation between characteristic and primitive variables is given by

$$\hat{\Phi} = T^{-1}\hat{q} \quad (10)$$

$$T^{-1} = \begin{bmatrix} -\bar{c}^2 & 0 & 0 & 0 & 1 \\ 0 & 0 & \bar{\rho}\bar{c} & 0 & 0 \\ 0 & 0 & 0 & \bar{\rho}\bar{c} & 0 \\ 0 & \bar{\rho}\bar{c} & 0 & 0 & 1 \\ 0 & -\bar{\rho}\bar{c} & 0 & 0 & 1 \end{bmatrix} \quad T = \begin{bmatrix} -1/\bar{c}^2 & 0 & 0 & 1/(2\bar{c}^2) & 1/(2\bar{c}^2) \\ 0 & 0 & 0 & 1/(2\bar{\rho}\bar{c}) & 1/(2\bar{\rho}\bar{c}) \\ 0 & 1/(\bar{\rho}\bar{c}) & 0 & 0 & 0 \\ 0 & 0 & 1/(\bar{\rho}\bar{c}) & 0 & 0 \\ 0 & 0 & 0 & 1/2 & 1/2 \end{bmatrix} \quad (11)$$

where  $\hat{\Phi} = [\hat{\phi}_1, \hat{\phi}_2, \hat{\phi}_3, \hat{\phi}_4, \hat{\phi}_5]$  are the characteristic variables. The solution vector for the inlet boundary is then composed as

$$\hat{q}_{bc} = T\hat{\Phi}_{bc} = T \begin{bmatrix} \hat{\phi}_1^+ \\ \hat{\phi}_2^+ \\ \hat{\phi}_3^+ \\ \hat{\phi}_4^+ \\ \hat{\phi}_5^- \end{bmatrix} \quad (12)$$

where '+' indicates the component was computed from information outside the domain(ex. User-specified pressure perturbation) and '-' indicates the component was computed from the interior solution.

Solid wall boundary conditions for the Euler equations require  $\vec{U} \cdot \vec{n} = 0$ . We require that the linearized components of velocity satisfy the same condition  $\vec{U}' \cdot \vec{n} = 0$ . Analyzing the normal component of the flux vector and applying the conditions  $\vec{U} \cdot \vec{n} = 0$  and  $\vec{U}' \cdot \vec{n} = 0$  gives

$$\vec{F} \cdot \vec{n} = \begin{pmatrix} \bar{\rho}(\vec{U}' \cdot \vec{n}) + \rho'(\vec{U} \cdot \vec{n}) \\ \bar{u}(\vec{U}' \cdot \vec{n}) + \frac{p'}{\bar{\rho}}n_x \\ \bar{v}(\vec{U}' \cdot \vec{n}) + \frac{p'}{\bar{\rho}}n_y \\ \bar{w}(\vec{U}' \cdot \vec{n}) + \frac{p'}{\bar{\rho}}n_z \\ \gamma\bar{p}(\vec{U}' \cdot \vec{n}) + p'(\vec{U} \cdot \vec{n}) \end{pmatrix} = \begin{pmatrix} 0 \\ \frac{p'}{\bar{\rho}}n_x \\ \frac{p'}{\bar{\rho}}n_y \\ \frac{p'}{\bar{\rho}}n_z \\ 0 \end{pmatrix} \quad (13)$$

This can be achieved by simply imposing  $\vec{U}' = 0$  such that the solution vector for a wall boundary is given as

$$\hat{q}_{bc} = \begin{bmatrix} \hat{p}^- \\ 0 \\ 0 \\ 0 \\ \hat{p}^- \end{bmatrix} \quad (14)$$

where '-' indicates the component was computed from the interior solution.

An absorbing layer based on the Perfectly Matched Layer(PML) concept was applied in this work to dampen outgoing waves from the computational domain.<sup>11,12</sup> The PML equations are then solved in a buffer region that surrounds the interior scheme. The PML equations are developed by making the following substitution in the original governing equations

$$\frac{\partial}{\partial x_j} \rightarrow \frac{1}{1 + \frac{i\sigma_j}{\omega}} \frac{\partial}{\partial x_j} = \frac{1}{\alpha_j} \frac{\partial}{\partial x_j} \quad (15)$$

where  $\sigma$  is a ramp function defined to increase smoothly from zero at the interface of the original equations and the PML equations and  $x_j$  is the  $j^{th}$  physical coordinate. It is defined as  $\sigma_j = \sigma_{max}|(x_j - x_{jb})/T|^2$ , where  $x_{jb}$  is the location of the Interior/PML interface and  $T$  is the thickness of the PML layer. Multiplying by  $\alpha_x\alpha_y\alpha_z$  for the linearized Euler equations gives

$$\alpha_y\alpha_z A \frac{\partial \hat{q}}{\partial x} + \alpha_x\alpha_z B \frac{\partial \hat{q}}{\partial y} + \alpha_x\alpha_y C \frac{\partial \hat{q}}{\partial z} + \alpha_x\alpha_y\alpha_z S_t = 0 \quad (16)$$

### II.C. Numerical flux

The local Lax-Friedrichs numerical flux is used for the element boundary integrals that provide coupling for the discontinuous elements. This is computed as

$$F^*(\mathbf{q}_L, \mathbf{q}_R) = \frac{1}{2}[F(\mathbf{q}_L) + F(\mathbf{q}_R) - |\alpha|_{max}(\mathbf{q}_L - \mathbf{q}_R)] \quad (17)$$

Here, the upwind dissipation term is multiplied by the value  $|\alpha|_{max}$ , which is the maximum eigenvalue associated with the mean flux jacobian. For this work,  $|\alpha|_{max}$  is computed as

$$|\alpha|_{max} = |\bar{U}_n| + \bar{c} \quad (18)$$

and  $\bar{U}_n$  is the magnitude of the face normal mean flow velocity.

### II.D. Duct modes

The pressure field in a duct can be decomposed into elementary modes associated with the duct geometry. These individual modes can then be analyzed to deduce their propagation characteristics through the duct and also their directivity patterns when radiating from a duct into free-space. To simulate acoustic radiation from a cylindrical duct, the modal profiles were computed and imposed as incoming pressure perturbations through the inlet boundary condition. The expansion of a pressure field in a cylindrical duct into modes at a given axial location is given as

$$p'(r, \theta) = \sum_{m=-\infty}^{\infty} \sum_{n=1}^{\infty} a_{mn} Re(\hat{p}_{mn}(r)e^{im\theta}) \quad (19)$$

where  $m$  is the azimuthal mode order and  $n$  is the radial mode order. These indices combined specify one particular mode  $(m, n)$ .  $\hat{p}_{mn}(r)$  is the radial profile associated with a given mode. For cylindrical ducts, it is computed as

$$\hat{p}_{mn}(r) = J_m\left(\alpha_{mn} \frac{r}{r_{max}}\right) \quad (20)$$

where  $J_m$  is a Bessel function of the first kind. The duct mode eigenvalue  $\alpha_{mn}$  is computed by imposing a physical boundary condition on the derivative of pressure at the duct wall as

$$\left. \frac{\partial p}{\partial r} \right|_{r=r_{max}} = J'_m(\alpha_{mn}) = 0 \quad (21)$$

The  $n^{th}$  value of  $\alpha_{mn}$  is computed by finding the  $n^{th}$  root of Equation (21).

### II.E. Solution technique

A common approach to solving Equation (6) is to add a pseudo-time term and then march the solution in pseudo-time until convergence is reached. As the pseudo-time derivative approaches zero, the original equation set is recovered. This traditional technique has two undesirable properties. First, the method generally requires many iterations until a converged solution is reached. Second, the pseudo time-stepping method can allow a well-known instability of the linearized Euler equations to corrupt the solution or cause the solution to diverge.<sup>8</sup>

The present work computes the solution in a fully-implicit manner, without the introduction of a pseudo-time term. This addresses the two undesirable properties of the pseudo time-stepping method. Specifically, the solution is obtained by solving a single linear system of equations and there is no mechanism for the physical instability to arise in the computation. The particular linear system of equations to be solved is constructed in the context of Newton's method. The formulation for Newton's method is

$$\frac{\partial R(Q)}{\partial Q} \Delta Q = -R(Q) \quad (22)$$

where  $R(Q)$  is the spatial residual from Equation 3 and  $\frac{\partial R(Q)}{\partial Q}$  is the matrix containing the linearization of the spatial scheme. Solving for  $\Delta Q$ , the solution is computed as

$$Q = Q_0 + \Delta Q \quad (23)$$

where  $Q_0$  is the initial solution vector.  $Q_0 = 0$  was used for this work. Computing the update vector  $\Delta Q$  requires the solution of a linear system of equations. This is accomplished with a flexible implementation of the Generalized Minimum Residual (FGMRES) algorithm coupled with a block-Jacobi or block-ILU0 preconditioner.

### II.F. Kirchhoff's method for far-field propagation

Kirchhoff's method was used to propagate near-field acoustic results to far-field observer locations for the problem of acoustic radiation from a cylindrical duct. A frequency-domain formulation from Lyrantzis and Mankbadi<sup>13,14</sup> is applied in this work as

$$\hat{p}(\vec{x}_o, \omega) = \frac{1}{4\pi} \int_{\Omega} e^{i\omega r/\bar{c}} \left[ \frac{1}{r} \left( -\frac{i\omega}{\bar{c}} \cos(\theta) \hat{p} - \frac{\partial \hat{p}}{\partial \mathbf{n}} \right) + \frac{\cos(\theta) \hat{p}}{r^2} \right] d\Omega \quad (24)$$

which is an integral over a surface containing the acoustic sources. Here,  $r$  is the distance from a source location on the Kirchhoff surface to the observer and  $\cos(\theta)$  is computed as  $\cos(\theta) = \vec{r} \cdot \vec{n}$  where  $\vec{r}$  is the unit vector in the direction of  $r$ . This integral is computed using the Gauss-Legendre quadrature routine within the DG-Chimera framework.

## III. Results

Two test cases were analyzed for this work to verify the implementation of the equations and the effectiveness of the DG-Chimera approach for these problems. These include an acoustic scattering problem with multiple rigid geometries and also an acoustic radiation problem from a cylindrical duct.

### III.A. Multi-geometry acoustic scattering

The problem of acoustic scattering from multiple rigid geometries was proposed as a benchmark problem in the Fourth Computational Aeroacoustics (CAA) Workshop on Benchmark Problems.<sup>15</sup> This problem was constructed to be a stringent test of the ability of computational codes to represent complex geometry. The problem consists of a Gaussian function applied as a pressure source, which interacts with multiple rigid cylinder geometries of different radii. An analytical solution exists for this problem so it provides a nice metric for comparison.<sup>16</sup>

The two rigid cylinder geometries have diameters of  $D_L = 1.0$  and  $D_R = 0.5$ . Their centers are located at  $(x, y) = (-4, 0)$  and  $(4, 0)$  respectively. The computational grid used for this problem is shown in Figure 1, which demonstrates the application of Chimera grids for representing complex geometries. Additionally, the half-cylinder grids representing the cylinder geometries use curved, quartic elements. The source term for this problem was defined as

$$S_u = \begin{bmatrix} 0 \\ 0 \\ 0 \\ 0 \\ \epsilon \end{bmatrix} \exp \left[ \frac{-\ln 2(x^2 + y^2)}{b^2} \right] \sin(\omega t) \quad (25)$$

where  $\epsilon = 0.4$ ,  $\omega = 8\pi$ , and  $b = 0.2$ . This calculation was run using a 7<sup>th</sup>-order accurate solution expansion. Because of symmetry, solid wall boundary conditions were used along the  $x$ -axis. Contours of the solution and the resulting acoustic scattering pattern are shown in Figure 2, which compares nicely with previously reported numerical results.<sup>17,18</sup> Additionally, the surface pressure on each cylinder was compared with the analytical solution. This is shown in Figure 3 and the comparison is nearly exact.

The multi-geometry acoustic scattering problem was run in two-dimensional (2D) form. There were 4850 2D elements used and this required 80 GB of working memory for the system matrix, block-ILU0 preconditioner, and supporting data using double-precision floating-point arithmetic. These resource requirements are well within the limits of current high-performance computing systems. This calculation executed in 2.2 hours using a single core of an Intel Xeon E5-2697 processor.

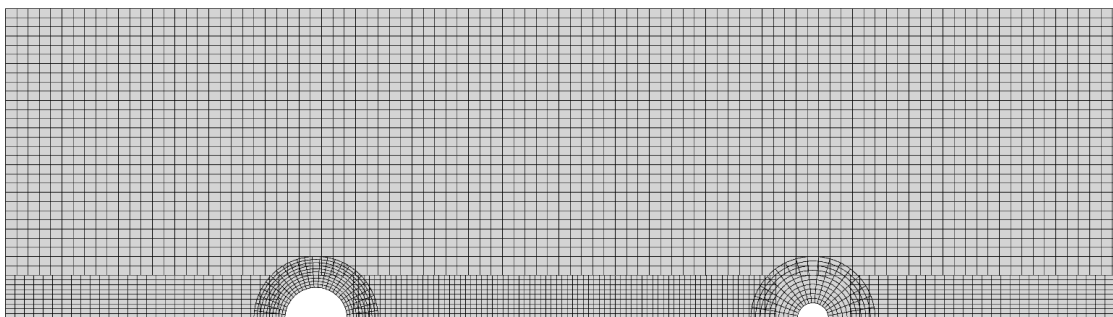


Figure 1. Computational grid - demonstrating Chimera overset grids.

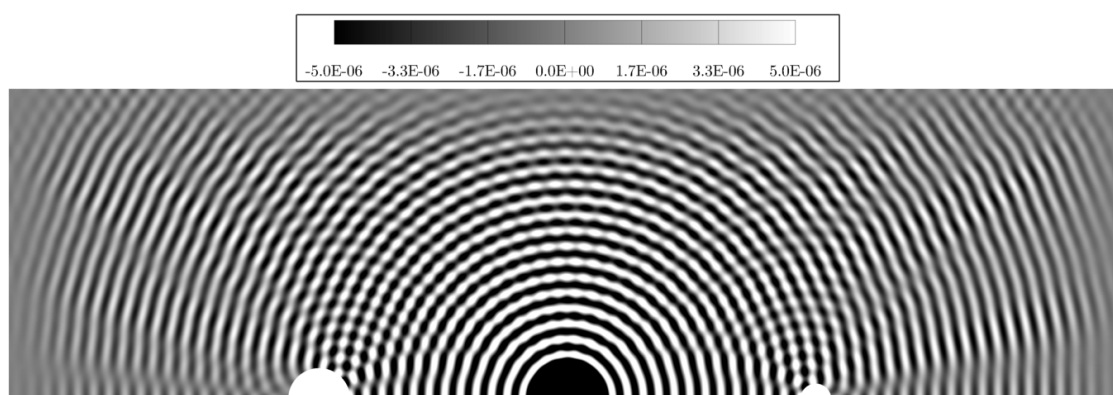
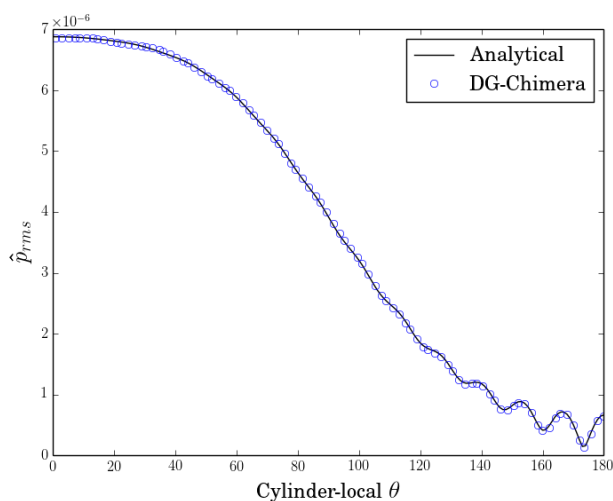
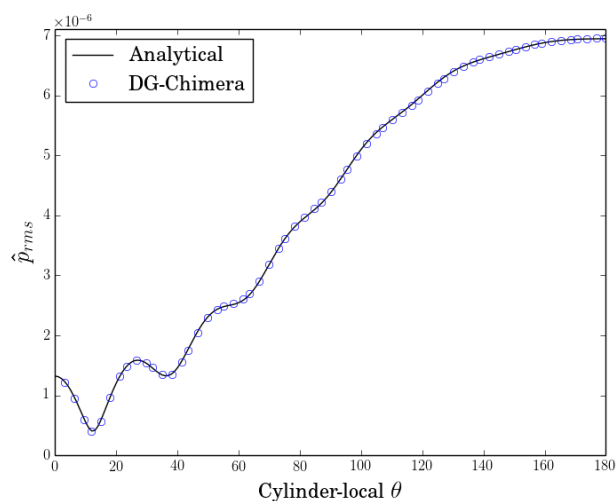


Figure 2. Real component of pressure perturbation -  $Re(\hat{p})$ .  $7^{th}$ -order accurate.



(a)  $\hat{p}_{rms}$  - Left Cylinder



(b)  $\hat{p}_{rms}$  - Right Cylinder

Figure 3. Comparison of predicted and analytical values for  $\hat{p}_{rms}$  on cylinder surfaces.



### III.B. Acoustic radiation from cylindrical duct

The problem of acoustic waves traveling through and radiating from cylindrical and annular ducts has been studied extensively by many researchers.<sup>2,19–21</sup> This problem is important for the analysis of noise radiating from jet engine inlet and exhaust systems. The unsteady flow fields associated with rotating turbomachinery components couple with duct modes, which are then transmitted through the engine and subsequently radiated into the surrounding space. This type of problem for the case of cylindrical ducts was analyzed by Munt,<sup>22</sup> who provided a derivation of an analytical solution.

This problem was analyzed here in a three-dimensional configuration (3D) to demonstrate the capability. It has been analyzed elsewhere using axisymmetric formulations of the governing equations,<sup>2,21</sup> which significantly reduces the computational resource requirements. The computational grid used in this study is shown in Figure 4(a). Curved, quartic elements are used to represent the geometry. An abutting, multi-block topology is used that demonstrates the utility of the Chimera technique applied with the DG method. Traditional Finite Volume-based Chimera implementations require a certain amount of overlap across grid blocks to maintain higher-order accuracy, which adds unnecessary complexity to the grid generation process. This overlap requirement is eliminated using a DG discretization.

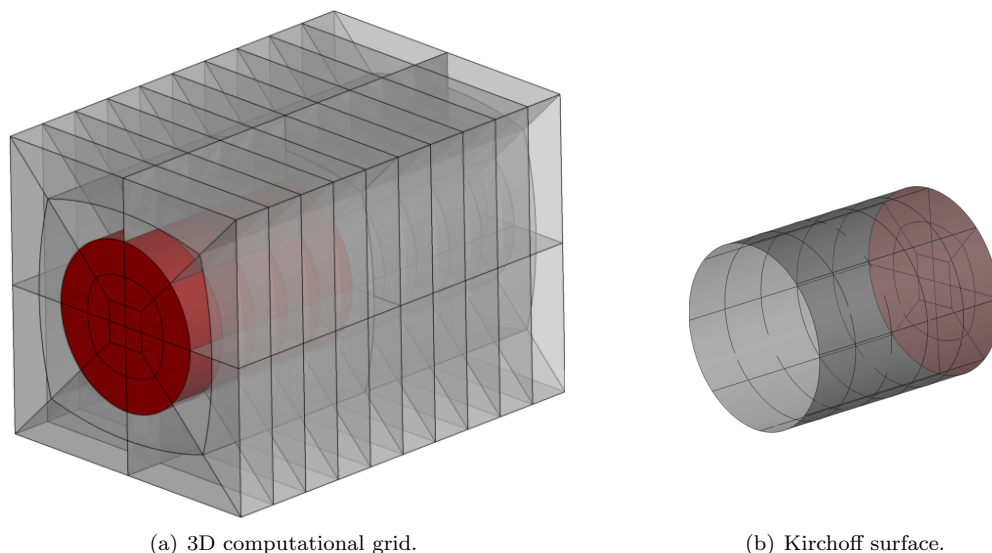


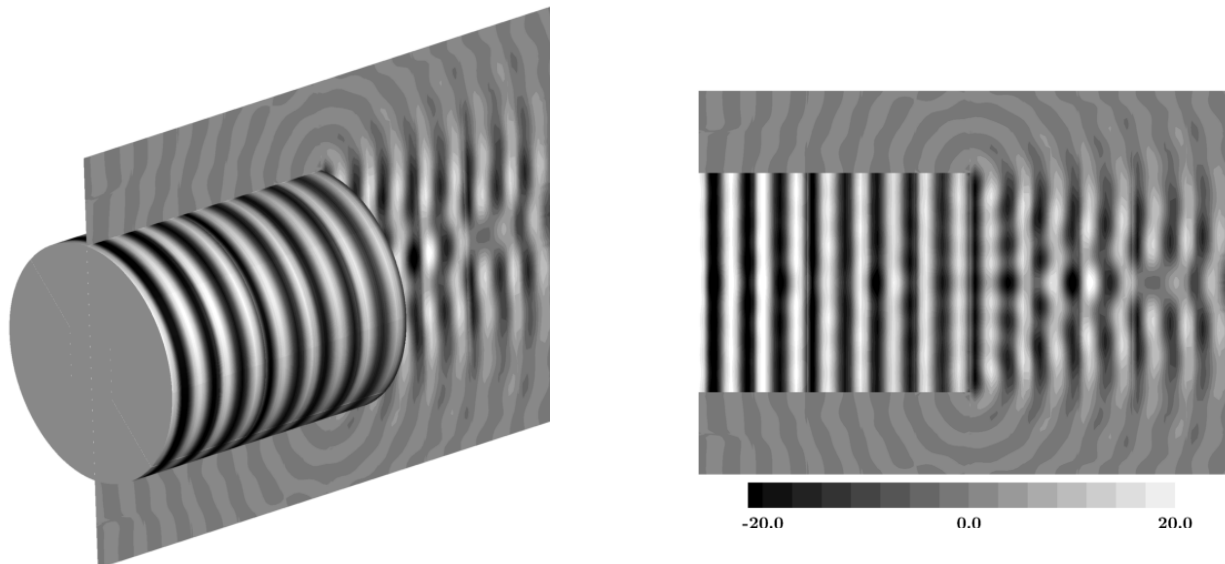
**Figure 4.** 3D grid for Munt acoustic radiation problem using quartic elements. Red-shaded elements indicate the interior of the duct.

A radius of 1.212 meters was used to specify the duct geometry. The mean flow conditions were  $\bar{c} = 340$  m/s,  $\bar{\rho} = 1.225$  kg/m<sup>3</sup>,  $\bar{M} = 0$ . The frequency was 956 Hz. Two configurations were investigated using the (0, 1) and (9, 1) modes as incoming perturbations of unit intensity. Kirchhoff's method was used to propagate the results to far-field observer locations along an arc 46 m from the center of the duct exit plane. The Kirchhoff surface used included the duct exit plane and the outer surface of the duct geometry, as shown in Figure 4(b). A PML layer with a thickness of 0.5 m was used to dampen waves exiting the domain. The results of far-field directivity for these cases were compared with analytical solutions. The analytical solutions used here to compare against were obtained from the report by Iob et al.<sup>2</sup> who attributed them to the Technische Universiteit Eindhoven.

The results for the (0, 1) mode case are shown in Figure 5. The plane wave travels through the duct and radiates into free-space. Both 6<sup>th</sup> and 7<sup>th</sup>-order accurate simulations were run. Due to low grid resolution, there is numerical attenuation of the duct mode traveling through the duct, which is non-physical. This is shown in the directivity of the radiated mode computed with Kirchhoff's method in Figure 6(c). The directivity pattern matches well with the analytical solution, however the amplitude is lower. The 7<sup>th</sup>-order calculation is improved over the 6<sup>th</sup>-order case, however grid resolution still too coarse to completely capture the wave propagation. The mode (9, 1) results are shown in Figure 6. Again, the far-field modal directivity pattern matches well with the analytical solution, however the amplitude is attenuated due to low grid resolution in the DG calculation. There is an unexpected extra lobe in the directivity pattern for the (9, 1) case near 0-degrees. It is likely that this is due to reflections of the waves either from the inlet boundary

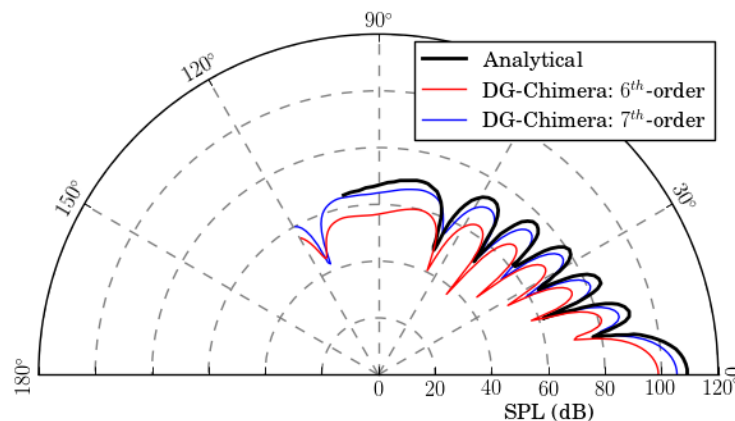
condition since it uses only 1D characteristic boundary conditions or from the PML layer, which is placed very close to the duct. This configuration is not optimal but was necessary because of memory constraints.

The discontinuous Galerkin method is known for being memory intensive for implicit problems due to the large number of degrees of freedom used to represent the solution. The 3D duct radiation problem was run using single precision floating-point arithmetic and required 180 GB of working memory for the system matrix, block-ILU0 preconditioner, and supporting data in the 7<sup>th</sup>-order accurate case. This memory requirement is significant but is within the limits of modern high-performance computing systems. The code used in the present work has not yet been parallelized so the memory requirement was challenging. However, for parallel codes, obtaining the necessary resources would be a more modest challenge.



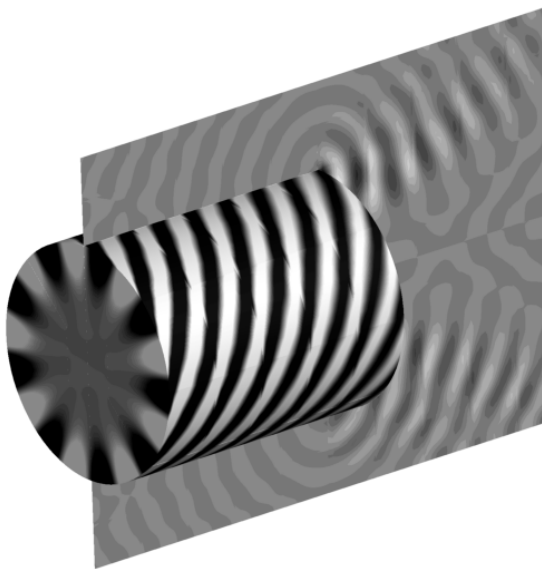
(a)  $Re(\hat{p})$  on 3D duct surface and center-plane slice.

(b)  $Re(\hat{p})$  on center-plane.

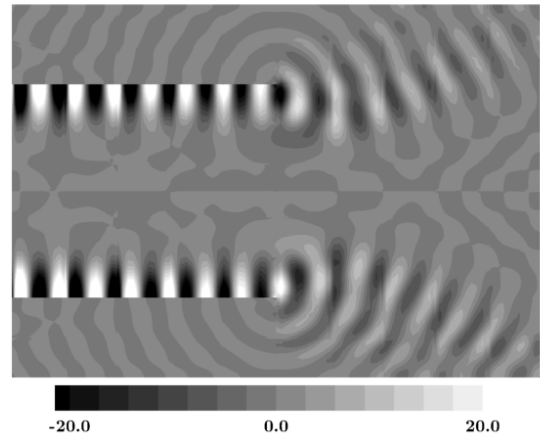


(c) Far-field directivity.

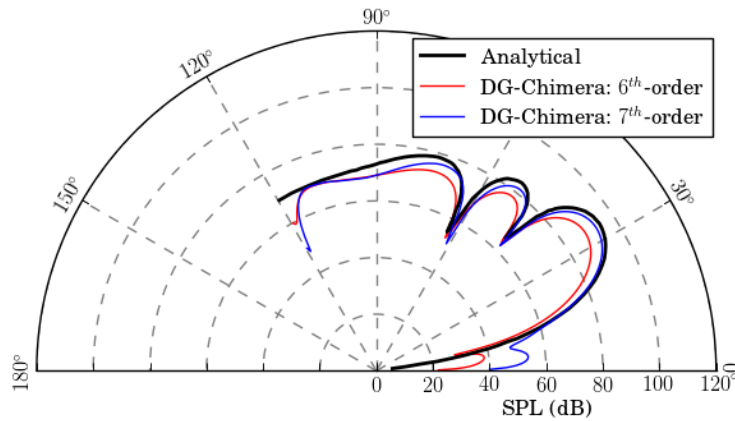
**Figure 5. Circular duct, mode(0,1),  $f = 956$  Hz. Contours show 7<sup>th</sup>-order solution.**



(a)  $Re(\hat{p})$  on 3D duct surface and center-plane slice.



(b)  $Re(\hat{p})$  on center-plane.



(c) Far-field directivity.

**Figure 6.** Circular duct, mode(9,1),  $f = 956$  Hz. Contours show 7<sup>th</sup>-order solution.

### III.B.1. Preconditioning

Newton-Krylov methods for solving linear systems depend strongly on preconditioning to achieve good performance for the iterative solver. Here we show the effect of block-Jacobi and block-ILU0 preconditioners compared with no preconditioner (Identity) for the time-linearized Euler system of equations. See Persson and Peraire<sup>23</sup> for more details on these preconditioners. The results presented here were obtained for the mode (0,1) duct radiation problem using a 6<sup>th</sup>-order accurate solution expansion. Figure 7 shows the effect of these preconditioners for the time-linearized Euler system of equations. It is shown that the block-Jacobi preconditioner is quite effective at improving convergence of the linear system solver for these simulations. The block-ILU0 preconditioner improves convergence even more, but this also requires additional overhead to construct and apply the preconditioner. The actual overhead is implementation dependent, so here we have strictly focused on the iteration count as a metric of comparison.

## IV. Conclusions

A fully-implicit implementation of the time-linearized Euler equations into a DG-Chimera solver was successfully carried out for the present study. A multi-geometry acoustic scattering problem was simulated to quantify the ability of the code to represent complex geometry and adequately resolve wave propagation

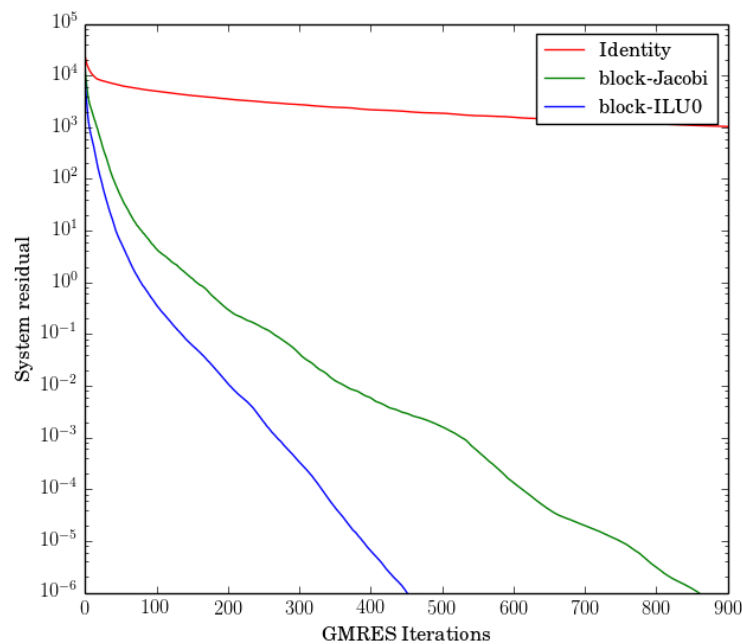


**Figure 7. Effect of preconditioners on GMRES convergence for the time-linearized Euler equations**

phenomena. Comparison of the numerical solution of pressure on the geometry surfaces against the analytical solutions was nearly exact. For the 2D case, it was found that the computational resource requirements of the fully-implicit algorithm are very manageable. Solutions of acoustic modes radiating from a cylindrical duct were also computed. Comparison of far-field propagated values of the numerical results with analytical solutions was good for the directivity pattern of the modes. However, the numerical solutions were attenuated due to low grid resolution in the original DG calculation. A block-Jacobi preconditioner was shown to be particularly effective at improving convergence of the GMRES iterative solver for the time-linearized Euler equations. A block-ILU0 preconditioner was also used and had a reduced iteration count compared to the block-Jacobi preconditioner but also increased computational overhead. The resources required by the 3D duct mode calculations are much more significant than the 2D calculations. However, the requirements are within the range of what is available on modern high-performance computing cluster. A parallel algorithm that is able to take advantage of those resources would make the 3D problem a tractable one.

## Acknowledgments

This material is based upon work supported by the National Science Foundation Graduate Research Fellowship Program under Grant No. 1102690. Special thanks to Dr. Scott Sherer from the Aerodynamic Technology Branch at Wright-Patterson Air Force Base for providing the analytical solution for the multi-geometry acoustic scattering benchmark problem.

## References

- <sup>1</sup>Hall, K. C., Lorence, C. B., and Clark, W. S., "Nonreflecting Boundary Conditions for Linearized Unsteady Aerodynamic Calculations," AIAA Paper 1993-0882, 1993.
- <sup>2</sup>Iob, A., Arina, R., and Schipani, C., "Frequency-Domain Linearized Euler Model for Turbomachinery Noise Radiation Through Engine Exhaust," *AIAA Journal*, Vol. 48, No. 4, 2010, pp. 848–858.
- <sup>3</sup>Bauer, M., Dierke, J., and Ewert, R., "Application of a Discontinuous Galerkin Method to Discretize Acoustic Perturbation Equations," *AIAA Journal*, Vol. 49, No. 5, May 2011, pp. 898–908.
- <sup>4</sup>Kelly, J. F. and Giraldo, F. X., "Continuous and discontinuous Galerkin methods for a scalable three-dimensional non hydrostatic atmospheric model: Limited-area mode," *Journal of Computational Physics*, Vol. 231, 2012, pp. 7988–8008.
- <sup>5</sup>Hartmann, R., Held, J., Leicht, T., and Prill, F., "Discontinuous Galerkin methods for computational aerodynamics - 3D adaptive flow simulation with the DLR PADGE code," *Aerospace Science and Technology*, Vol. 14, 2010, pp. 512–519.
- <sup>6</sup>Wukie, N. A. and Orkwis, P. D., "A implicit, discontinuous Galerkin Chimera solver using automatic differentiation,"

AIAA Paper 2016-2054, 2016.

<sup>7</sup>Galbraith, M. D., *A Discontinuous Galerkin Chimera Overset Solver*, Dissertation, University of Cincinnati, 2013.

<sup>8</sup>Agarwal, A., Morris, P. J., and Mani, R., "Calculation of Sound Propagation in Nonuniform Flows: Suppression of Instability Waves," *AIAA Journal*, Vol. 42, No. 1, 2004, pp. 80–88.

<sup>9</sup>Campobasso, M. S. and Giles, M. B., "Computing Linear Harmonic Unsteady Flows in Turbomachines with Complex Iterative Solvers," AIAA Paper 2005-4705, 2005.

<sup>10</sup>Rao, P. P. and Morris, P. J., "Use of Finite Element Methods in Frequency Domain Aeroacoustics," *AIAA Journal*, Vol. 44, No. 7, 2006, pp. 1643–1652.

<sup>11</sup>Hu, F. Q., "On Absorbing Boundary Conditions for Linearized Euler Equations by a Perfectly Matched Layer," *Journal of Computational Physics*, Vol. 129, No. 1, November 1996, pp. 201–219.

<sup>12</sup>Hu, F. Q., "A Stable, Perfectly Matched Layer for Linearized Euler Equations in Unsplit Physical Variables," *Journal of Computational Physics*, Vol. 173, No. 2, November 2001, pp. 455–480.

<sup>13</sup>Lyrantzis, A. S. and Mankbadi, R. R., "Prediction of the Far-Field Jet Noise Using Kirchhoff's Formulation," *AIAA Journal*, Vol. 34, No. 2, February 1996, pp. 413–416.

<sup>14</sup>Lyrantzis, A. S., "Surface integral methods in computational aeroacoustics - From the (CFD) near-field to the (Acoustic) far-field," *International Journal of Aeroacoustics*, Vol. 2, No. 2, April 2003, pp. 95–128.

<sup>15</sup>Visbal, M., "Multi-Geometry Scattering Problem: Category 2, Complex Geometry," Proceedings of the fourth computational aeroacoustics workshop on benchmark problems, NASA/CP-2004-212954, 2004.

<sup>16</sup>Sherer, S. E., "Acoustic Scattering From Multiple Circular Cylinders: Category 2, Problems 1 and 2, Analytical Solution," Proceedings of the fourth computational aeroacoustics workshop on benchmark problems, NASA/CP-2004-212954, 2004.

<sup>17</sup>Sherer, S. E. and Visbal, M. R., "Computational Study of Acoustic Scattering from Multiple Bodies Using a High-Order Overset Grid Approach," AIAA Paper 2003-3203, 2003.

<sup>18</sup>Iob, A., Rinaldi, R. D. R., and Arina, R., "A Frequency-Domain Linearized Euler Model for Noise Radiation," *Aeronautics and Astronautics*, edited by M. Mulder, chap. 6, InTech, Rijeka, 2011, pp. 159–184.

<sup>19</sup>Zhang, X., Chen, X. X., and Morfey, C. L., "Acoustic radiation from a semi-infinite duct with a subsonic jet," *International Journal of Aeroacoustics*, Vol. 4, No. 1-2, January 2005, pp. 169–184.

<sup>20</sup>Huang, X., Chen, X., Ma, Z., and Zhang, X., "Efficient Computation of Spinning Modal Radiation Through an Engine Bypass Duct," *AIAA Journal*, Vol. 46, No. 6, June 2008, pp. 1413–1423.

<sup>21</sup>Özyörük, Y., "Numerical prediction of aft radiation of turbofan tones through exhaust jets," *Journal of Sound and Vibration*, Vol. 325, No. 1-2, August 2009, pp. 122–144.

<sup>22</sup>Munt, R. M., "The interaction of sound with a subsonic jet issuing from a semi-infinite cylindrical pipe," *Journal of Fluid Mechanics*, Vol. 83, No. 4, December 1977, pp. 609–640.

<sup>23</sup>Persson, P.-O. and Peraire, J., "Newton-GMRES Preconditioning for Discontinuous Galerkin Discretizations of the Navier-Stokes Equations," *Journal on Scientific Computing*, Vol. 30, No. 6, October 2008, pp. 2709–2733.

<sup>24</sup>Galbraith, M. C., Allmaras, S. R., and Darmofal, D. L., "A Verification Driven Process for Rapid Development of CFD Software," AIAA Paper 2015-0818, 2015.

<sup>25</sup>Galbraith, M. C., Benek, J. A., Orkwis, P. D., and Turner, M. G., "A discontinuous Galerkin Chimera scheme," *Computers and Fluids*, Vol. 98, 2014, pp. 27–53.

<sup>26</sup>Orkwis, P. D. and McRae, D. S., "Newton's Method Solver for High-Speed Viscous Separated Flowfields," *AIAA Journal*, Vol. 30, 1992, pp. 78–85.